



One-step controllable synthesis of amorphous $(\text{Ni-Fe})\text{S}_x/\text{NiFe(OH)}_y$ hollow microtube/sphere films as superior bifunctional electrocatalysts for quasi-industrial water splitting at large-current-density

Qijun Che, Qing Li*, Ya Tan, Xinhong Chen, Xi Xu, Yashi Chen

School of Chemistry and Chemical Engineering, Southwest University, Chongqing 400715, PR China



ARTICLE INFO

Keywords:

Bifunctional electrocatalysts
One-step co-deposited mechanism
amorphous $(\text{Ni-Fe})\text{S}_x/\text{NiFe(OH)}_y$
quasi-industrial water splitting
large current density

ABSTRACT

Crystalline transition-metal chalcogenides with (oxy)-hydroxides hybrids multiple nanoarchitectures are a new type of promising bifunctional electrocatalysts for electrolysis of water, but their amorphous states are scarcely studied. Herein, a facile electrodeposited approach is presented to fabricate hierarchically amorphous $(\text{Ni-Fe})\text{S}_x/\text{NiFe(OH)}_y$ films on Nickel foam. By accurately tuning multi-components and electrochemical-parameters resulting in abundant micro-tube/sphere morphologies and phase evolution to obtain unique amorphous nano-cluster architectures, the $(\text{Ni-Fe})\text{S}_x/\text{NiFe(OH)}_y$ catalyst performs super electrocatalytic performance, driving the current density of $100 \text{ mA}\cdot\text{cm}^{-2}$ at ultralow overpotential of 124 mV and 290 mV for hydrogen and oxygen evolution reaction in 1 M KOH solution with first-class long-term stability for at least 50 h , respectively. In addition, the bimetallic Ni-Fe sulfides and NiFe hydroxides are confirmed to be highly-intrinsic active components for HER and OER. More importantly, the $(\text{Ni-Fe})\text{S}_x/\text{NiFe(OH)}_y$ material directly as cathode and anode electrodes, achieves $10 \text{ mA}\cdot\text{cm}^{-2}$ at low electrolytic voltage of 1.46 V in 1 M KOH , even at large current density of $1200 \text{ mA}\cdot\text{cm}^{-2}$ only needing 2.2 V as well as super-durability at $1000 \text{ mA}\cdot\text{cm}^{-2}$ for 50 h in quasi-industrial conditions. Further experimental results reveal that both temperature and appropriate alkalinity are in favour of reducing the overall hydrolytic overpotential due to accelerating sluggish thermodynamics and dynamics. Parallelly, the bifunctional $(\text{Ni-Fe})\text{S}_x/\text{NiFe(OH)}_y$ electrode is one of the best efficient electrocatalysts in alkaline electrolyte up to now and expected for large-scale industrial water-splitting at large-current-density.

1. Introduction

Large-scale industrial production of hydrogen and oxygen by electrocatalytic water splitting is universally considered as the most promising approaches to address environmental pollution and energy depletion [1,2]. In this process, due to the sluggish kinetics and unfavorable thermodynamics (theoretical electrolytic voltage of 1.23 V) of two half-reactions: anodic multi-electron oxygen evolution reaction (OER) and cathodic two-electron hydrogen evolution reaction (HER) [3,4], highly-efficient and robust electrode materials are urgently crucial to speed up the reaction rate and lower the high total overpotential [5,6]. Temporarily, noble Pt-based catalysts for their best HER activity and Ru/Ir-based oxides are been well-known to be benchmark for OER, but their evident drawbacks limit blown-up commercial applications, including high cost, low earth-abundance and poor adhesion with substrates (e.g., carbon cloth; glassy carbon; nickel foam) as well as low stability (during the water oxidation) [7–9]. Contrarily, the novel

developed electrocatalysts on the basis of transition metal-based materials are more blossoming and promising, including chalcogenides [10–12], carbides [13–15], phosphides [16–18], borides [19,20] and metal-free hybrids [21,22] for HER; whereas oxides [23–25], (oxy)hydroxides [26,27], phosphates [28], and perovskites [29] toward the OER. In spite of significant advances have been made lately either for HER or OER in electrocatalysis fields, very few of these electrocatalysts reported nowadays are able to highly-effective drive both the HER and OER in same electrolyte. Because almost promising noble-free HER and OER electrocatalysts perform at different pH condition [30,31]; such as most of HER catalysts work well in acid media, even two or three order of magnitudes than in basic media [32], while OER catalysts work better in neutral or alkaline environments. Besides, to meet the practical needs of industrial electrolyzers operating at high current density ($\geq 1 \text{ A}\cdot\text{cm}^{-2}$), unfortunately only a few works explored OER catalysts [7] at this highly-harsh conditions but lack of HER catalysts, let alone bifunctional catalysts. Therefore, the searching of earth-abundant and

* Corresponding author at: School of Chemistry and Chemical Engineering, Southwest University, Chongqing 400715, PR China.
E-mail address: liqingswu@163.com (Q. Li).

cost-efficient bifunctional electrocatalysts for overall water electrolysis satisfying both of above two key points simultaneously is still a worldwide challenge [31,33].

Aimed to achieve the large-current-density electrolysis of water, an affordable bifunctional electrocatalyst should simultaneously meet multiple requirements: (I) Highly-intrinsic active sites for both HER and OER; (II) earth-abundant raw materials with low costs; (III) simple ambient-temperature synthesis methods for avoiding high temperature ($\geq 300^\circ\text{C}$) to reduce expensive equipment costs and the operating risks; (IV) easy close to reactants with satisfied wettability such as super-hydrophilicity to fast remove gas bubbles from the surface of the electrodes; (V) strong adhesion with the current collectors to prevent the catalytically active phase from peeling off; (VI) steady long-term durability against corrosion at high current density especially during the strong oxidizing process. Nevertheless, up to now, it is still a huge difficulty to seek an appropriate bifunctional electrocatalyst for fulfilling above standards. It is true that a powdered catalyst has to be anchored on the current collectors (e.g., glassy carbon) by a polymer-binder to obtain electrodes. For this case, a common problem of the active phase peeling off would take place when current density exceeds $\sim 80 \text{ mA}\cdot\text{cm}^{-2}$, getting worse at higher current density ($\geq 500 \text{ mA}\cdot\text{cm}^{-2}$). Notably, the stability of electrocatalysts directly responds to the structural integrity of active materials further related to an important parameter of faraday efficiency whether there are other side reactions taking place besides the sole HER or OER. At this point, promising transition-metal chalcogenides [34–36] and phosphides [37–40] as the bifunctional electrocatalysts for overall water-splitting have been reported, but the strong oxidation peaks (approximately at $1.4 \sim 1.5 \text{ V}$ vs. RHE) generally occurred. Large reduction peaks [35,37] in which current density even arrived at about $-100 \text{ mA}\cdot\text{cm}^{-2}$ also took place under the OER process, resulting in reduced activity of catalysts or deactivation along with poor stability especially at high-current-density.

Based on above analysis, designing earth-abundant, low-cost, and self-supported micro/nano-bifunctional catalysts with ultrahigh intrinsic HER and OER activities, high electro-conductibility, super-hydrophilicity, and high structural stability are worth pursuing toward our goal for meeting low-energy consumption at large current density. For HER, previous density functional theory (DFT) calculations identified that both metals and sulfur species of single metallic chalcogenides are active sites [41]; further bimetallic materials performed better due to synergistic effects [12,42]. Particularly, recently researchers found amorphous materials are more efficient compared with their crystalline counterparts [4,20,43,44]. For OER, although it is a lot of controversy for transition-metal chalcogenides whether themselves as the OER active sites or in situ newly-formed oxides during the oxygen evolution process [35,45,46], there is no doubt that Ni-based bimetallic hydroxides have been proved to be one of the most efficient OER electrocatalysts by both DFT calculations and experimental evidences [26,47,48], and newly reported their amorphous states worked better but still need further improvement [7,49]. Thus, highly-active bifunctional electrocatalysts can be realized by integrating amorphous bimetallic chalcogenides with hydroxides hybrid on self-supported collector.

Herein, for the first time we report one-step facile electrodeposited synthesis of amorphous $(\text{Ni}-\text{Fe})\text{S}_x/\text{NiFe(OH)}_y$ micro-tube/sphere films on highly conductive nickel foam (NF) at room temperature suitable for both HER and OER at large-current-density. This cost-efficient and stable electrocatalytic activity of $(\text{Ni}-\text{Fe})\text{S}_x/\text{NiFe(OH)}_y$ is attributed to accurately morphological controls and the unique amorphous structures. The amorphous bimetallic Ni-Fe sulfides optimize electronic structures at atom-level and thus promote HER kinetics; the amorphous bimetallic Ni-Fe hydroxides provide key intrinsic OER active sites. The synergistic effects of bimetallic Ni-Fe sulfides and hydroxides at nanoscale further improved both HER and OER performance. In addition, the micro/nano hierarchical architectures not only expose more dual-active sites, but also promote gas evacuation by providing a super-

aerophobic interface under the electrolyte. As anticipated, the bifunctional $(\text{Ni}-\text{Fe})\text{S}_x/\text{NiFe(OH)}_y$ catalyst offers super HER and OER activity as well as durability with ultralow overpotential of 124 mV and 290 mV at $100 \text{ mA}\cdot\text{cm}^{-2}$, respectively. Moreover, for overall water splitting, the $(\text{Ni}-\text{Fe})\text{S}_x/\text{NiFe(OH)}_y$ catalyst achieved a low voltage of 1.46 V at $10 \text{ mA}\cdot\text{cm}^{-2}$ in 1.0 M KOH solution, even large current density of $1200 \text{ mA}\cdot\text{cm}^{-2}$ at 2.2 V along with super durability at $1000 \text{ mA}\cdot\text{cm}^{-2}$ for 50 h in quasi-industrial conditions, expecting for large-scale industrial hydrolysis.

2. Experimental section

2.1. Chemicals and reagents

Ni foams (Thickness: 0.5 mm; areal density: 280 g m^{-2}) were purchased from Kunshan dessco Electronics Co., Ltd. Nickel sulfate hexahydrate ($\text{NiSO}_4\cdot6\text{H}_2\text{O}$), thiourea ($\text{CH}_4\text{N}_2\text{S}$), trisodium citrate dehydrate ($\text{Na}_3\text{C}_6\text{H}_5\text{O}_7\cdot2\text{H}_2\text{O}$) and hydrochloric acid (HCl, 37 wt %) were purchased from Chengdu Kelong Chemical Reagent Factory. Iron nitrate nonahydrate ($\text{Fe}(\text{NO}_3)_3\cdot9\text{H}_2\text{O}$) was purchased from Aladdin. Ruthenium oxide (RuO_2) and nafion solution (5 wt %) were bought from Shanghai Macklin Biomedical Co., Ltd. Potassium hydroxide (KOH) and ethanol ($\text{C}_2\text{H}_5\text{OH}$) were bought from China Chongqing Chuandong Chemical Ltd. The RuO_2 -NF electrode was prepared according to a previously reported method [40].

2.2. Synthesis of hollow $(\text{Ni}-\text{Fe})\text{S}_x/\text{NiFe(OH)}_y$ micro-tube/sphere films

A piece of foursquare Ni foam (1 cm^{-2}) was cleaned ultrasonically in ethanol (20 mL) and in 3 M HCl solution (10 mL) for 20 min each, and then subsequently washed with deionized water several times to remove the surface impurities and dried by filter paper. The $(\text{Ni}-\text{Fe})\text{S}_x/\text{NiFe(OH)}_y$ microtube films (mass loading (ML): $2.9 \text{ mg}\cdot\text{cm}^{-2}$) were *in situ* supported on the NF substrates via electrodeposition at $\sim 30^\circ\text{C}$. The electrodeposition was conducted in a conventional three-electrode cell with the cleaned NF, Pt sheet and a saturated calomel electrode (SCE) as the working, auxiliary, and reference electrodes, respectively. The electroplating bath contained 0.1 M $\text{NiSO}_4\cdot6\text{H}_2\text{O}$, 0.1 M $\text{Na}_3\text{C}_6\text{H}_5\text{O}_7\cdot2\text{H}_2\text{O}$, 0.9 M $\text{CH}_4\text{N}_2\text{S}$ and 0.01 M $\text{Fe}(\text{NO}_3)_3\cdot9\text{H}_2\text{O}$. The experiment was then carried out by constant current electrodeposition at $-80 \text{ mA}\cdot\text{cm}^{-2}$ for 360 s. The as-deposited samples were washed with DI water and dried in air. To optimize the compositions, the additional moles of Fe^{3+} in the electrolyte set as 5 mM (denote: FNS-LDH-5, ML: $2.8 \text{ mg}\cdot\text{cm}^{-2}$), 10 mM and 15 mM (denote: FNS-LDH-15, ML: $3.0 \text{ mg}\cdot\text{cm}^{-2}$), respectively. Interestingly, the different moles of Fe^{3+} can also effectively modulate the morphology. We found the 10 mM Fe^{3+} yields the $(\text{Ni}-\text{Fe})\text{S}_x/\text{NiFe(OH)}_y$ films with the highest HER and OER catalytic activity. In order to further accurately alter morphology, setting up three kinds of current densities adopting 0.01 M Fe^{3+} in the electrolyte bath were -40, -80 and $-100 \text{ mA}\cdot\text{cm}^{-2}$ (denote: FNS-LDH-40 (ML: $2.8 \text{ mg}\cdot\text{cm}^{-2}$), $(\text{Ni}-\text{Fe})\text{S}_x/\text{NiFe(OH)}_y$, FNS-LDH-100 (ML: $3.1 \text{ mg}\cdot\text{cm}^{-2}$), respectively) without others parameter variation.

2.3. Synthesis of nonstoichiometric $\text{Ni}_{0.96}\text{S}$ films with rich defects

The $\text{Ni}_{0.96}\text{S}$ films (ML: $2.85 \text{ mg}\cdot\text{cm}^{-2}$) were also obtained by room-temperature (30°C) electrodeposition. Typically, the electrolyte bath comprised of 0.1 M $\text{NiSO}_4\cdot6\text{H}_2\text{O}$, 0.1 M $\text{Na}_3\text{C}_6\text{H}_5\text{O}_7\cdot2\text{H}_2\text{O}$ and 0.9 M $\text{CH}_4\text{N}_2\text{S}$. The galvanostatic electrodeposition was conducted at $-80 \text{ mA}\cdot\text{cm}^{-2}$ for 6 min.

2.4. Synthesis of defective nanosheets $\text{Fe}_{0.96}\text{S}/\text{Fe}(\text{OH})_3$ films

The $\text{Fe}_{0.96}\text{S}/\text{Fe}(\text{OH})_3$ (ML: $2.88 \text{ mg}\cdot\text{cm}^{-2}$) was prepared via the same method of that $\text{Ni}_{0.96}\text{S}$ using 0.01 M Fe^{3+} to replace the Ni^{2+} keeping others electrochemical parameters unaltered.

2.5. Synthesis of bimetallic NiFe–OH films

The Bimetallic NiFe–OH (ML: 2.84 mg·cm⁻²) was synthesized by electrodeposition method. The electrolyte bath comprised of 0.01 Fe³⁺, 0.1 M Ni²⁺ and 0.1 M Na₃C₆H₅O₇·2H₂O. The electrochemical conditions were the same as that of nonstoichiometric Ni_{0.96}S Films.

2.6. Synthesis of ferric hydroxide films

The ferric hydroxide (ML: 2.79 mg·cm⁻²) was synthesized by electrodeposition pathway using single metal ion Fe³⁺ (0.01 M) in the electrolyte bath with the constant current at -80 mA·cm⁻² for 360 s at ~30 °C.

2.7. Materials characterization

SEM (S-4800, Hitachi, Japan; in 10 kV) was used to characterize the morphology of as-prepared samples and corresponding EDS analyzed elementary contents and distribution. TEM (JEM-2100 F, Japan; in 200 kV) was acquired to probe the structure of materials. Powder XRD was performed on a Purkinje General Instrument XD-6 with Cu K α radiation ($\lambda = 0.15406$ nm). XPS measurement was determined on Thermo ESCALAB 250 with Al K α electronic gun and calibrated with C 1 s (284.9 eV). Raman Spectrum was performed by RFS 100/S10400.

2.8. Electrochemical measurements

Electrochemical measurements were performed by electrochemical workstation on SC350 (Wuhan Kwsite Instrument Co., Ltd.) in a standard three-electrode system. The as-prepared self-supported samples were used directly as working electrodes without further treatments in the alkaline medium. Graphite rod and a saturated calomel electrode (SCE) were used as counter and reference electrodes, respectively. For the HER measurements, the potentiodynamic polarization curves were conducted at the voltage vs. SCE from open circuit voltages to -1.6 V at a scan rate of 2 mV s⁻¹. For the OER tests, the potentiodynamic scan was from open circuit to 0.8 V. In this study, all the potentials were converted to the referring to the reversible hydrogen electrode (RHE, saturated KCl) following equation: $E_{RHE} = E_{SCE} + 0.241 + 0.059 \text{ pH}$, unless stated otherwise [2]. All electrochemical data were not iR-compensation.

2.9. Electrochemical active surface area

According to the literature [50], the electrochemical active surface area (ECAS) was obtained from double layer capacitance (C_{dl}) at range non-Faradaic potentials window in 1 M KOH by using cyclic voltammetry (CV). In detail, the difference values ($j_{\text{anodic}} - j_{\text{cathodic}}$) at median window potential from CV data plotted against the scan rates to conduct linear fitting, whose slope is equal-to-twice of the C_{dl} which is proportional to the effective electrochemical surface area. Only the several key as-synthesized samples were considered to carry out for ECAS performance.

2.10. Electrochemical impedance spectroscopy (EIS)

EIS for different materials synthesized was performed from 100 kHz to 0.01 Hz with the amplitude of 10 mV at the overpotentials of -80 mV under the HER operating condition.

3. Results and discussion

3.1. Formed mechanism and characterization

The fabrication of the amorphous (Ni–Fe)S_x/NiFe(OH)_y material is systematically taken into account by one-step electrochemical

deposited pathway. Firstly, the binary crystalline nickel sulfide nanoparticles are effective for hydrogen evolution while poor for oxygen evolution (Scheme 1). Because sulfur-anion species may only play a “pre-catalysis” role during the water oxidation demonstrated by Mabayoje et al. [46]. Secondly, to achieve highly catalytic oxygen evolution, Fe-based hydroxides with conductive Fe_{0.96}S hybrids are necessary (Scheme 1). Besides, the bimetallic (oxy)hydroxides may be beneficial toward HER [51]. Integrating above points on single current collector (NF), the bifunctional (Ni–Fe)S_x/NiFe(OH)_y catalysts can be constructed. The formation mechanism of amorphous (Ni–Fe)S_x was followed by formula (1)–(4) [52–54]. In brief, the Ni²⁺ and reduced Fe²⁺ reacted with local generated S²⁻ ions on the cathode surfaces to form nickel-iron sulfides. The amorphous NiFe(OH)_y was obtained according to formula (5) and (6) [55,56]. The NO₃⁻ ions were reduced at the electrode surface with the aid of electrons to generate hydroxide ions, and then reacted with Ni²⁺ and Fe³⁺ ions to form bimetallic hydroxides deposited on the cathodes.

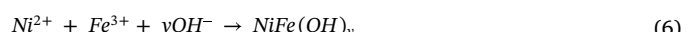
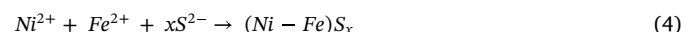
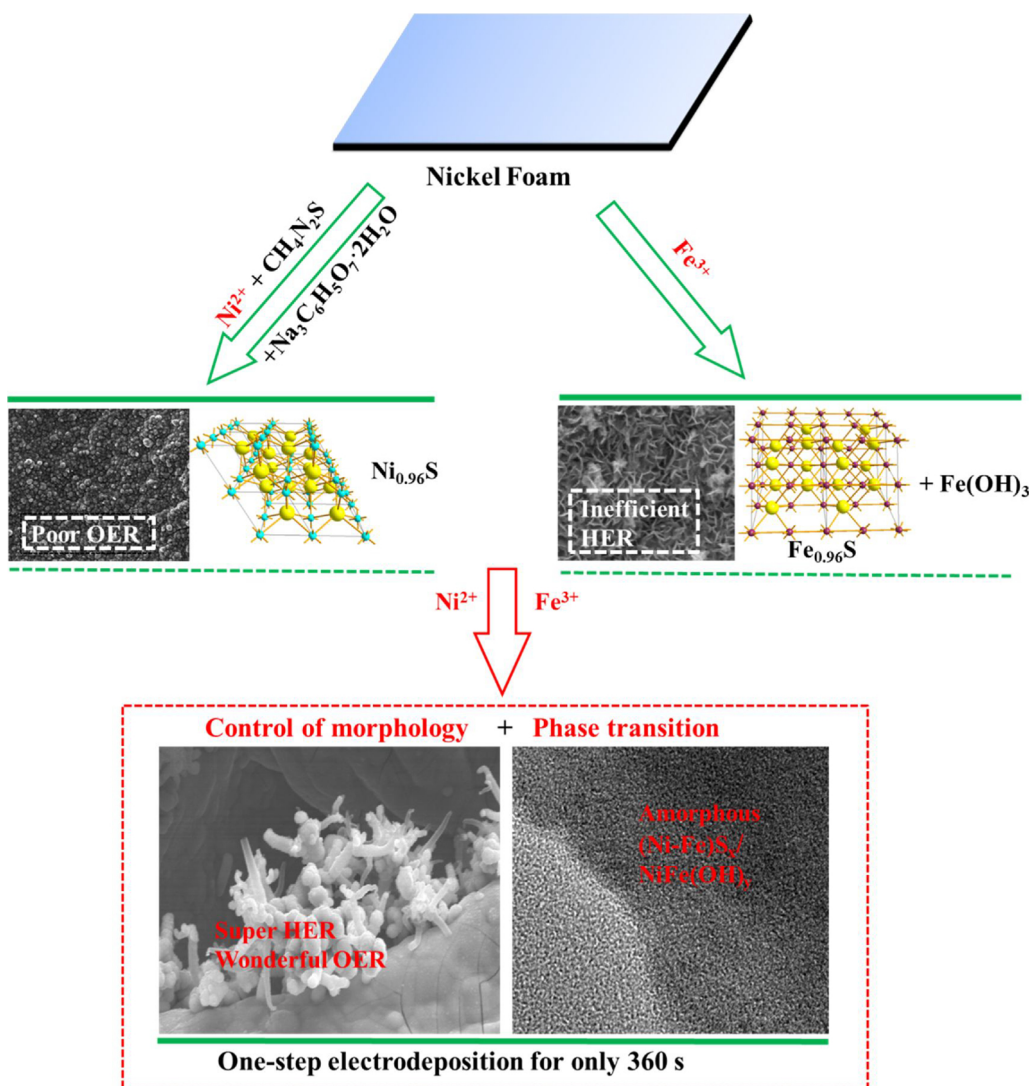


Fig. 1(A–C) presented the scanning electron microscopy (SEM) images of non-integer stoichiometric Ni_{0.96}S films uniformly covering the NF, which displayed large micro-cracks (red cycles) and the roughly surface composed of many nano-particles. For advantages, these cracks can expose rich HER active sites and provide paths for gas release. For disadvantages, the catalytic phase may peel off from NF at large current density and thus resulting in deactivation. In addition, the energy-dispersive X-ray spectroscopy (EDS) images (Fig. 1D) showed homogeneous distribution of Ni_{0.96}S for Ni and S elements. As the Fig. 1(E–G) shown, using Fe(NO₃)₃·9H₂O as precursor to replace NiSO₄·6H₂O, the morphology of Fe_{0.96}S/Fe(OH)₃ displayed roughly similar “bubbles” shapes Films (Fig. 1E, red cycles) made up of ultrathin nano-sheets (thickness: about 6–10 nm) with corresponding EDS mapping uniform distribution for Fe, S, and O elements. Significantly, when Ni²⁺, Fe³⁺ and NO₃⁻ ions in electropolating solution, the morphology of (Ni–Fe)S_x/NiFe(OH)_y catalyst (Fig. 1I) showed great differences at NF skeleton edges and based plane. For edges (Fig. 1J), there were rich hollow micro-tubes and micro-spheres intertwining with each other. The formation of these features can be attributed to “tip discharge” effects and appropriate addition of Fe³⁺ ions precursor. To explore “tip discharge” effects, setting up three different current densities of -40, -80 and -100 mA·cm⁻², the SEM images (Figure S1) of the products revealed that unique hollow structures were converted from single micro-tubes to micro-spheres with the increase of current density. In addition, the concentrations of Fe³⁺ ions also played a vital role. With the Fe³⁺ ions precursor increased (5, 10 and 15 mM), the morphology features were changed from micro-spheres to hollow micro-tubes (Figure S2). As for based planes (Fig. 1L), there were many tiny micro-cracks and micro-spheres which consisted of vast nano-particles. Similarly, these tiny micro-cracks were under the control of current density and the amount of Fe³⁺ ions. To sum up, these “lug boss” edges at NF skeleton are favorable to generate “tip discharge”. By properly adjusting the current density and concentration of Fe³⁺ ions, we successfully realized precise controls of hollow micro-tubes/spheres morphologies. Further EDS mapping analysis at NF edges (Fig. 1K) and based plane (Fig. 1M) for Ni, Fe, S and O elements were revealed distributing the entire material. In addition, the micro/nano-architectures of (Ni–Fe)S_x/NiFe(OH)_y possessed excellent wettability under the water with the contact angle (CA)



Scheme 1. Schematic illustration of control of morphology and phase evolution of the $(\text{Ni-Fe})\text{S}_x/\text{NiFe}(\text{OH})_y$.

$\leq 0^\circ$ (Figure S3), indicating its super-aerophobic property which is in favour of facilitating gas (H_2 and O_2) desorption on catalytic surfaces during the electrochemical reaction [57,58].

The powder X-ray diffraction (PXRD) pattern and transmission electron microscopy (TEM) along with high-resolution TEM (HR-TEM) were conducted to determine chemical structure of $(\text{Ni-Fe})\text{S}_x/\text{NiFe}(\text{OH})_y$. As the Figure S4 shown, the PXRD pattern of as-prepared Ni-S sample only detected a broad diffraction peak at approximately 45.6° , which is consistent with the strongest peak of non-integer stoichiometric $\text{Ni}_{0.96}\text{S}$ (JCPDS no. 50-1791), manifesting weak crystallinity. After Fe^{3+} replacing Ni^{2+} precursor, the PXRD pattern probed a weak peak at 43.8° in agreement with the strongest peak of $\text{Fe}_{0.96}\text{S}$ (JCPDS no. 50-1788). No noticeable XRD signals of Fe-OH were detected, indicating the amorphous features [56]. When both Ni^{2+} and Fe^{3+} were precursors, the as-obtained catalyst was detected a broad "steamed bread" peaks at about 45° by PXRD diffraction, which may be form amorphous phase. As the Fig. 2(A, B, C) presented, the HR-TEM images verified rich point/line defects as well as weak crystallinity with interplanar spacing of 0.196 nm corresponding to the $(1\ 0\ 2)$ plane of $\text{Ni}_{0.96}\text{S}$. As the Fig. 2(D-F) shown, the $\text{Fe}_{0.96}\text{S}/\text{Fe}(\text{OH})_3$ catalyst consisted of amorphous $\text{Fe}(\text{OH})_3$ and low crystalline $\text{Fe}_{0.96}\text{S}$ with interplanar spacing of 0.207 nm correlating to the $(1\ 0\ 2)$ plane. Obviously rich defects with tortuous lattice fringes, the crystalline and amorphous phase interfaces (Fig. 2F) may provide extra active sites and thus

accelerating electrochemical reaction especially for OER [11,27,59]. As the Fig. 2(G-I) shown, the HR-TEM images of $(\text{Ni-Fe})\text{S}_x/\text{NiFe}(\text{OH})_y$ composites carefully scratched off from the NF substrate proved amorphous features with no detection of typical lattice fringes. The inset image (Fig. 2I) was the fast fourier transformation (FFT) pattern, further manifesting amorphous characteristics.

The Raman spectra and X-ray photoelectron spectroscopy (XPS) measurements were carried out to further confirm the chemical structure, compositions and valence states of $(\text{Ni-Fe})\text{S}_x/\text{NiFe}(\text{OH})_y$ catalysts. As presented in Fig. 3A, there were no characteristic Raman peaks for NF substrates. The comparison of nickel sulfide possessed characteristic Raman bands at $183, 222, 290, 306$, and 350 cm^{-1} in agreement with the literature [60]. Another compared sample of $\text{Fe}_{0.96}\text{S}/\text{Fe}(\text{OH})_3$ displayed the similar near-Raman bands as that of nickel sulfide (soft pink rectangle) due to the similarity of structures. As the additional broad Raman bands in the wavenumber range from 550 to 750 cm^{-1} displayed, the Raman center-band at 685 cm^{-1} can be attributed to Fe^{3+} -O vibrations in the disordered Fe-OH clusters [7,61]. Compared with nickel/iron sulfide in the same Raman bands districts, the peaks of $(\text{Ni-Fe})\text{S}_x/\text{NiFe}(\text{OH})_y$ evidently changed to be weak and wide due to the disorders of structure. In addition, in the 550 cm^{-1} to 750 cm^{-1} regions, there were obvious evidences that the center position at 650 cm^{-1} of $(\text{Ni-Fe})\text{S}_x/\text{NiFe}(\text{OH})_y$ was red-shifted compared with $\text{Fe}(\text{OH})_3$ (685 cm^{-1}), indicating forming out-of-order bimetallic

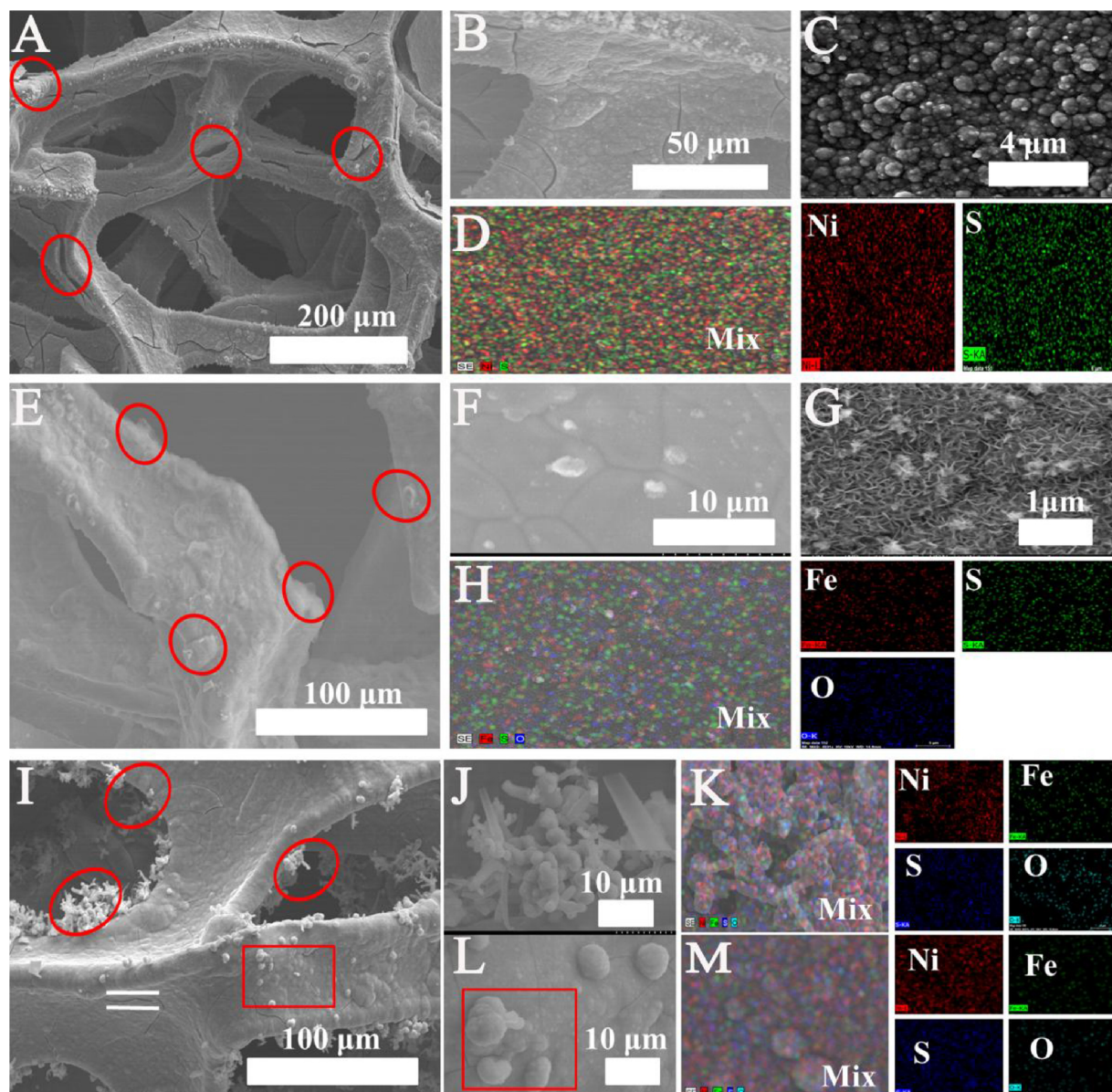


Fig. 1. (A–C) SEM images of $\text{Ni}_{0.96}\text{S}$ with corresponding (D) EDS elemental mapping for Ni and S. (E–G) SEM images of $\text{Fe}_{0.96}\text{S}/\text{Fe}(\text{OH})_3$ with related (H) EDS elemental mapping for Fe, S and O. (I) SEM images of $(\text{Ni-Fe})\text{S}_x/\text{NiFe}(\text{OH})_y$ at NF skeleton edges (J, red circle) and based plane (L, red rectangle) along with corresponding (K, M) EDS elemental mapping images (For interpretation of the references to colour in this figure legend, the reader is referred to the web version of this article).

hydroxide nanoclusters, possibly on account of dopant effect of Ni atom in the films [7,62]. The further characterization of the structure was studied by the XPS. As the Fig. 3B shown, the full spectrum of amorphous $(\text{Ni-Fe})\text{S}_x/\text{NiFe}(\text{OH})_y$ proved the presence of Ni, Fe, S, O, and C (for calibration) elements. Fig. 3C and D were the high resolution XPS spectra of Ni 2p and Fe 2p, respectively. For Ni 2p region, the two peaks at 855.7 and 873.4 eV were attributed to Ni 2p_{3/2} and Ni 2p_{1/2}, respectively [63], which indicated that the existence form of Ni in the composites was Ni²⁺ oxidation state [64]. For Fe 2p region, there were four peaks: two fitted in the Fe 2p_{3/2} (711.7 eV, 712.4 eV) and another two in the Fe 2p_{1/2} (722.7 eV, 725.2 eV) regions, which can be explained coexistence of Fe²⁺ and Fe³⁺ species [27,65,66]. For S 2p (Figure S5 A) region, the binding energy at ~163.7 and ~162.1 eV indicated typically bimetallic sulfides with S²⁻ species; center peak at ~168.1 eV was related to a higher oxide state consistent with previous reports [10,12]. The O 1s region (Figure S5B) was attributed to the adsorbed O₂, metal-O and O-H species [67]. Above evidences fully

certified the $(\text{Ni-Fe})\text{S}_x/\text{NiFe}(\text{OH})_y$ catalysts were made up of amorphous bimetallic Ni-Fe-S and Ni-Fe-OH.

3.2. HER activity and mechanism

The electrocatalytic HER performance was investigated by a standard three-electrode system in 1 M KOH (pH = 14) solution. The prepared samples were directly used as the working electrodes. As the Fig. 4A shown, $\text{Fe}_{0.96}\text{S}/\text{Fe}(\text{OH})_3$ catalyst displayed enhanced HER activity ($\eta_{100} = 366$ mV) in comparison to bare NF ($\eta_{100} = 522$ mV) due to rich defects of nonstoichiometric $\text{Fe}_{0.96}\text{S}$ to enhance conductivity along with amorphous $\text{Fe}(\text{OH})_3$ which has been reported possibly hydrogen evolution active sites [51]. The weak crystalline $\text{Ni}_{0.96}\text{S}$ significantly lowered HER overpotential ($\eta_{100} = 157$ mV) expressing typical transition-metal chalcogenides for active HER features. Further, the enriched point/line defects not only efficiently exposed HER active sites, but also may induce charge-redistribution thus to greatly promote

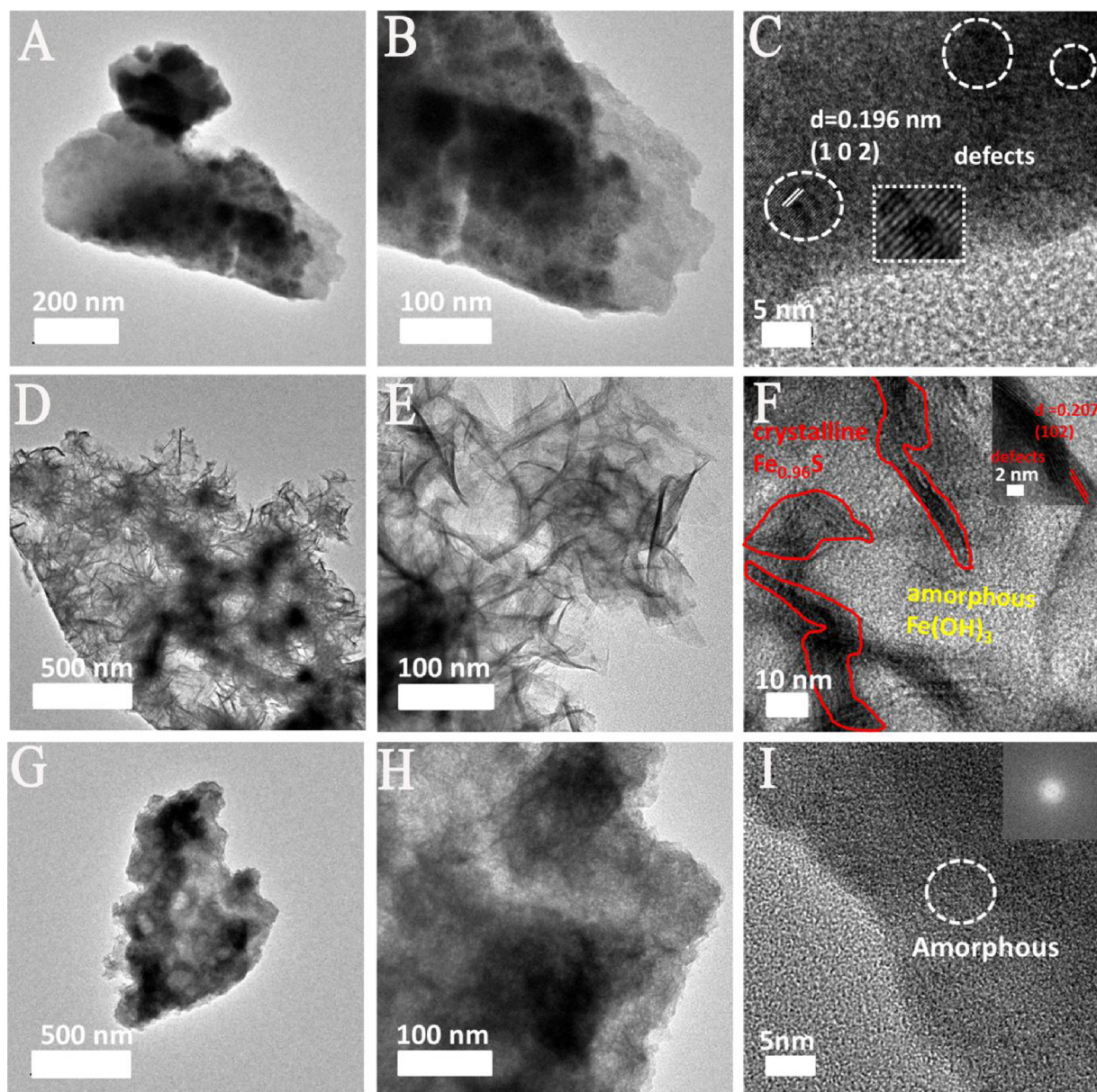


Fig. 2. TEM images with different magnifications of (A–C) $\text{Ni}_{0.96}\text{S}$, (D–F) $\text{Fe}_{0.96}\text{S}/\text{Fe}(\text{OH})_3$, and (G, H, I) $(\text{Ni}-\text{Fe})\text{S}_x/\text{NiFe}(\text{OH})_y$ catalysts, inset : FFT pattern.

electrochemical reduction reaction [11,68]. However, although the defective nonstoichiometric $\text{Ni}_{0.96}\text{S}$ was firstly reported to high-efficiently generate hydrogen superior to most of other transition-metal chalcogenides (Table S1), the HER overpotential at large-current-density was still high (e.g., $\eta_{300} = 275 \text{ mV}$) unsuitable for currently industrial applications. Conversely, on the basis of nickel sulfide to availably introduce iron element to obtain amorphous $(\text{Ni}-\text{Fe})\text{S}_x/\text{NiFe}(\text{OH})_y$ catalysts, this composites vastly enhanced HER performance with ultra-low overpotential of 124 mV at $100 \text{ mA}\cdot\text{cm}^{-2}$ even at higher-current-density of $242 \text{ mA}\cdot\text{cm}^{-2}$ ($\eta_{242} = 156 \text{ mV}$) outstripping noble Pt sheets (Fig. 4A), fully indicating multielemental synergistic effects in favour of providing rich HER active sites. It is true that the Pt wire/sheets still needed high overpotential while current density are in excess of $100 \text{ mA}\cdot\text{cm}^{-2}$ reported by L.Yu et al. [63]. In addition, we tried our best to utilize DFT caculations to acquire more inner informations, but fell through due to the complexity of the amorphous structures [69]. Such an outstanding alkaline catalyst may be explained unique amorphous cluster structures of short-range order but long-range disorder [32], optimal compositions along with morphology, and thus systematically

speeding up hydrodynamics and thermodynamics.

To probe the impacts of amount of additional Fe^{3+} precursor, we set up 5, 10 and 15 mM $\text{Fe}(\text{NO}_3)_3 \cdot 9\text{H}_2\text{O}$ precursor in the electrobath, labeled as FNS-LDH-5, $(\text{Ni}-\text{Fe})\text{S}_x/\text{NiFe}(\text{OH})_y$, FNS-LDH-15, respectively. Obviously the moderate Fe contents (10 mM) showed the best performance (Fig. 4A) compared with both FNS-LDH-5 ($\eta_{100} = 157 \text{ mV}$) and FNS-LDH-15 ($\eta_{100} = 175 \text{ mV}$) in agreement with previous report [70]. Here the further EDS (Figure S6) was conducted to analyze atomic percent of FNS-LDH-5, $(\text{Ni}-\text{Fe})\text{S}_x/\text{NiFe}(\text{OH})_y$ and FNS-LDH-15, respectively. With the increase of Fe^{3+} precursor, it was certain to make metal-hydroxides go up but result in low conductivity. The optimal atomic ratio of Fe/Ni is 0.255 (Table S2) showing the best HER activity. It is well-known that the conductivity of electrocatalysts has straightly impact on electrochemical activity. The competitions between enhanced Fe-active-sites and reduced conductivity by appropriate amount of Fe-doping made maximized benefits. In addition, to further explore the hollow micro-tubes/spheres morphology from “tip discharge” for hydrogen evolution activity, setting up galvanostatic parameter of -40, -80, and $-100 \text{ mA}\cdot\text{cm}^{-2}$, the as-obtained samples labeled as FNS-LDH-

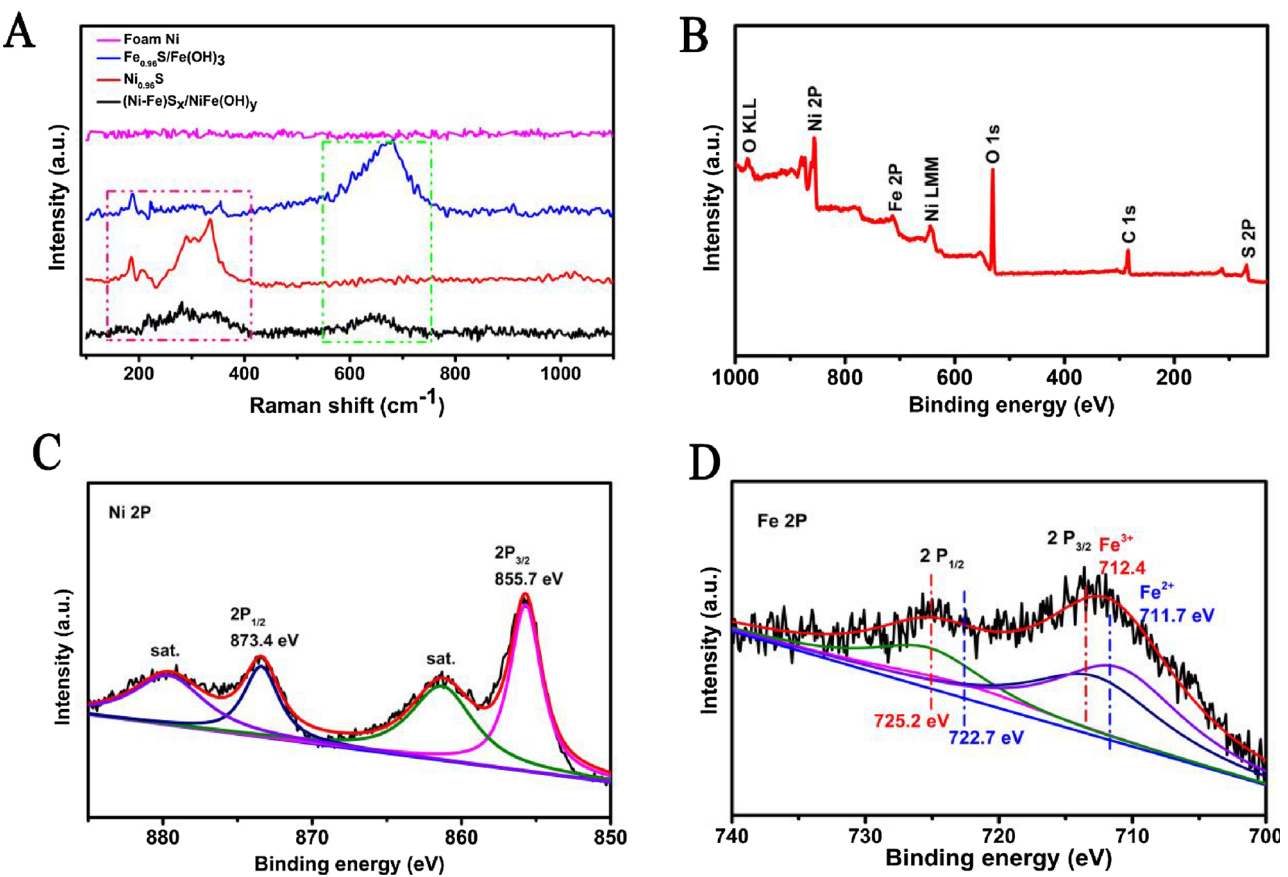
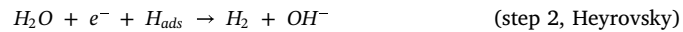


Fig. 3. (A) Raman spectra of Ni foam, $\text{Fe}_{0.96}\text{S}/\text{Fe}(\text{OH})_3$, $\text{Ni}_{0.96}\text{S}$, and $(\text{Ni}-\text{Fe})\text{S}_x/\text{NiFe}(\text{OH})_y$ catalysts. The XPS spectra of (B) sum peaks, (C) Ni 2 P, (D) Fe 2 P of $(\text{Ni}-\text{Fe})\text{S}_x/\text{NiFe}(\text{OH})_y$.

40, $(\text{Ni}-\text{Fe})\text{S}_x/\text{NiFe}(\text{OH})_y$, and FNS-LDH-100, respectively. From thunderstorm nature “tip discharge”, the rugged NF skeleton edges under the action of electrons brought forth similar phenomena. With the increase of current density, the morphology (Figure S1 and Fig. 1(L, K)) transformed from tiny hollow micro-tubes to micro-spheres. As the Fig. 4B displayed, the intertwined micro-tube/sphere $(\text{Ni}-\text{Fe})\text{S}_x/\text{NiFe}(\text{OH})_y$ was superior to both FNS-LDH-40 ($\eta_{100} = 208 \text{ mV}$) and FNS-LDH-100 ($\eta_{100} = 148 \text{ mV}$), which may be attributed to unparalleled morphology providing larger exposed active area.

Furthermore, the HER kinetics of the as-synthesized catalysts was studied by the Tafel plots and electrochemical impedance spectroscopy (EIS). Correlatively, the exchange current density (j_0) can be obtained by Tafel formula ($\eta = a + b \log j_0$, a , b and j present over-potential, intercept, Tafel slope and current density, respectively) [71]. Typically, under the alkaline conditions, the HER mechanisms can be described by Volmer-Heyrovsky or Volmer-Tafel following three principle steps [19]:



Theoretically, the Tafel slopes of step 1, step 2, and step 3 are identified to be 118, 39, and 29 mV decade⁻¹ at 25 °C, respectively [72]. As shown in Fig. 4C, $\text{Ni}_{0.96}\text{S}$ and $\text{Fe}_{0.96}\text{S}/\text{Fe}(\text{OH})_3$ displayed Tafel slopes of 97 and 175 mV decade⁻¹ along with j_0 of 1.4 and 0.75 mA·cm⁻², respectively, indicating that the Volmer (water discharge) reaction was rate-limiting step for both of two. Contrastingly, the amorphous $(\text{Ni}-\text{Fe})\text{S}_x/\text{NiFe}(\text{OH})_y$ composite exhibited a smaller Tafel slope of 68 mV decade⁻¹ and larger j_0 value of 3.3 mA·cm⁻² close to the Pt sheets (54 mV decade⁻¹, j_0 of 3.5 mA·cm⁻²), demonstrating that the HER occurred on $(\text{Ni}-\text{Fe})\text{S}_x/\text{NiFe}(\text{OH})_y$ surface via a Volmer-Heyrovsky

mechanism. The Heyrovsky reaction appears to be dominant rate-limiting step. In addition, previously theoretical DFT evidence by Z. Zhu et al. manifested [67], introduction of metal-hydroxides (e.g., $\text{Co}(\text{OH})_2$) onto binary 2D-MoS₂/WS₂ surface can effectively lower the kinetic energy barrier of the water dissociation step. Similarly, in the $(\text{Ni}-\text{Fe})\text{S}_x/\text{NiFe}(\text{OH})_y$ composite, the synergistic effects of between $(\text{Ni}-\text{Fe})\text{S}_x$ and $\text{NiFe}(\text{OH})_y$ at nano/atomic-scale may effectively accelerate sluggish kinetics. Fig. 4D showed the Nyquist plots and the corresponding equivalent circuit of several key samples. On the basis of radius of the semicircular Nyquist plots by Zview software fitting, the charge transfer resistance (R_{CT}) of $\text{Ni}_{0.96}\text{S}$ and $\text{Fe}_{0.96}\text{S}/\text{Fe}(\text{OH})_3$ were calculated to be 0.705 and 80.903 Ω (Table S3), respectively. This result well explained that the $\text{Fe}_{0.96}\text{S}/\text{Fe}(\text{OH})_3$ exhibited poor HER activity due to non-conductive amorphous $\text{Fe}(\text{OH})_3$ resulting in such a larger R_{CT} to hinder charge transfer. Although the $(\text{Ni}-\text{Fe})\text{S}_x/\text{NiFe}(\text{OH})_y$ catalyst displayed R_{CT} of 0.957 Ω slightly higher than defective $\text{Ni}_{0.96}\text{S}$ because of existence of bimetallic hydroxides, the two difference of 0.252 Ω can almost leave out. Such low resistance resulted in favorable HER kinetics.

To assess electrochemical active surface area (ECSA), the double-layer capacitance (C_{dl}) which is positive correlation of the ECSA was carried out by cyclic voltammetry (CV) method (Figure S7). As shown in Fig. 4E, the C_{dl} value of $(\text{Ni}-\text{Fe})\text{S}_x/\text{NiFe}(\text{OH})_y$ was 1.51 mF·cm⁻² larger than $\text{Ni}_{0.96}\text{S}$ (0.845 mF·cm⁻²) and $\text{Fe}_{0.96}\text{S}/\text{Fe}(\text{OH})_3$ (0.675 mF·cm⁻²), indicating that $(\text{Ni}-\text{Fe})\text{S}_x/\text{NiFe}(\text{OH})_y$ possessed the highest ECSA in three samples. Generally the larger C_{dl} was, the lower HER overpotential became. However, the C_{dl} value of $(\text{Ni}-\text{Fe})\text{S}_x/\text{NiFe}(\text{OH})_y$ was not high in comparison to many literatures [73–75]. We hypothesised that intrinsic activity density of $(\text{Ni}-\text{Fe})\text{S}_x/\text{NiFe}(\text{OH})_y$ resulted in such a low overpotential. Therefore, the real Brunauer-Emmett-Teller (BET) surface area was measured (Figure S8). There were few differences of the BET surface area based on tested results. Further

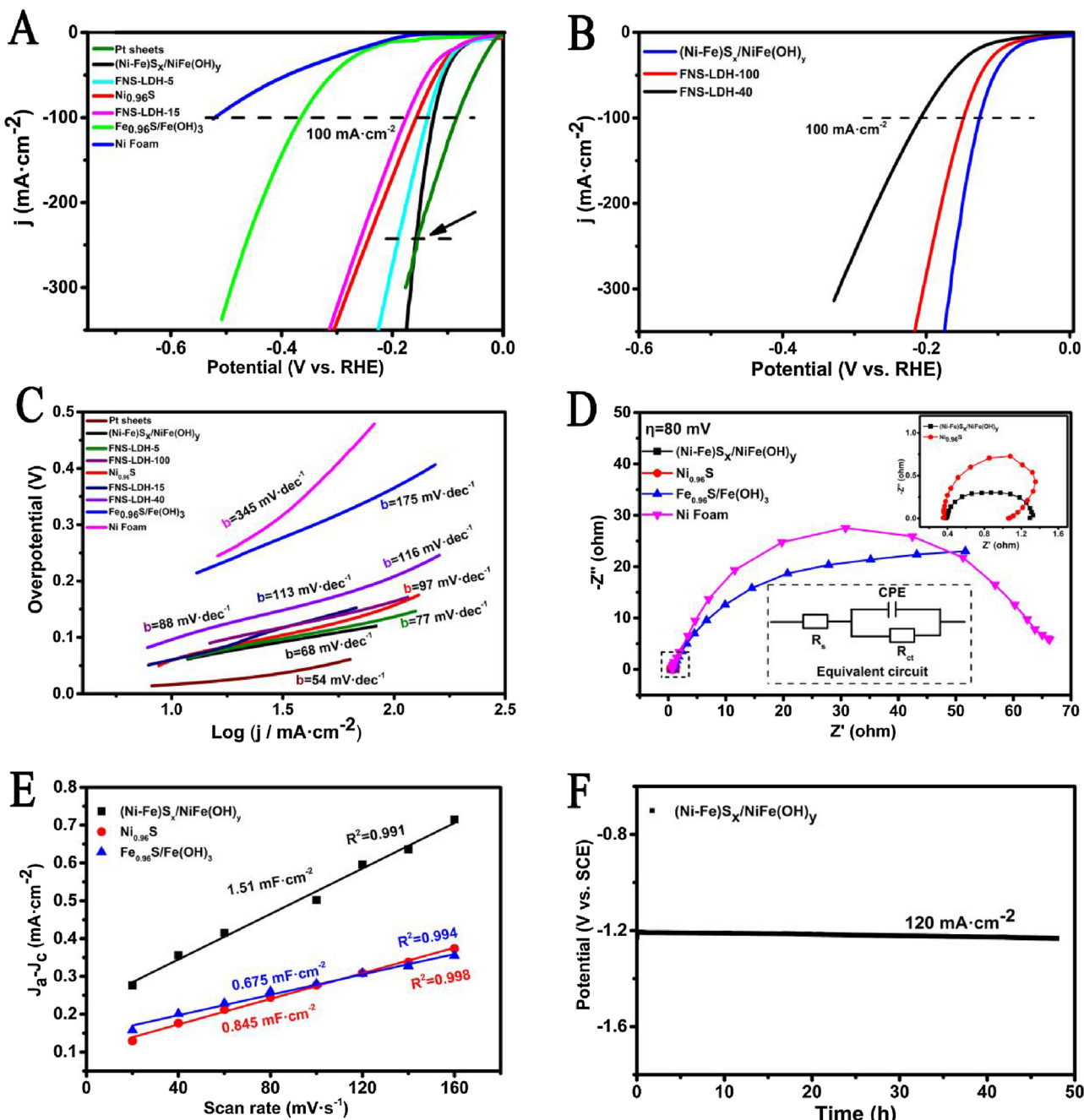


Fig. 4. The HER performance in 1 M KOH solution without iR-compensation. (A, B) Polarization curves for (Ni-Fe)S_x/NiFe(OH)_y, FNS-LDH-5, Ni_{0.96}S, FNS-LDH-15, Fe_{0.96}S/Fe(OH)₃, Ni Foam, commercial Pt sheets, FNS-LDH-100, and FNS-LDH-40. (C) corresponding Tafel plots of the as-prepared samples. (D) Electrochemical impedance spectra (EIS) at overpotential of 80 mV for several key samples, inset: circuit fitting. (E) Capacitive currents plotted against scan rates for (Ni-Fe)S_x/NiFe(OH)_y, Ni_{0.96}S, and Fe_{0.96}S/Fe(OH)₃ catalysts to assess electrochemical active surface area (ECSA). (F) Long-term stability of (Ni-Fe)S_x/NiFe(OH)_y recorded at constant current density of $-120 \text{ mA}\cdot\text{cm}^{-2}$ for 48 h.

mass activity (MA) also confirmed this conjecture. As the Figure S9 exhibited, among them, the (Ni-Fe)S_x/NiFe(OH)_y showed the highest MA ($91.43 \text{ mA}\cdot\text{mg}^{-1}$) values. In addition, to meet requirements of industrial hydrogen production at large-current-density, the long-lasting durability of catalysts played a indispensable role. As shown in Fig. 4F, the (Ni-Fe)S_x/NiFe(OH)_y exhibited super stability at fixed large current density of $-120 \text{ mA}\cdot\text{cm}^{-2}$ for 48 h with negligible activity decay. After long-term durability, the (Ni-Fe)S_x/NiFe(OH)_y catalyst still kept well its morphology (Figure S10).

3.3. OER activity and mechanism

The catalytic activity toward OER of (Ni-Fe)S_x/NiFe(OH)_y was also investigated in 1 M KOH solution. For comparative aims, several samples including NF, commercial RuO₂, Ni_{0.96}S, Fe_{0.96}S/Fe(OH)₃, FNS-LDH-5, FNS-LDH-15 along with NiFe-OH and Fe(OH)₃ (Figure S11) were also studied under the same alkaline condition. Notably the powder RuO₂ had to be deposited on a NF-support by using a polymer-binder (Nafion) as working electrode. Fig. 5A showed typical

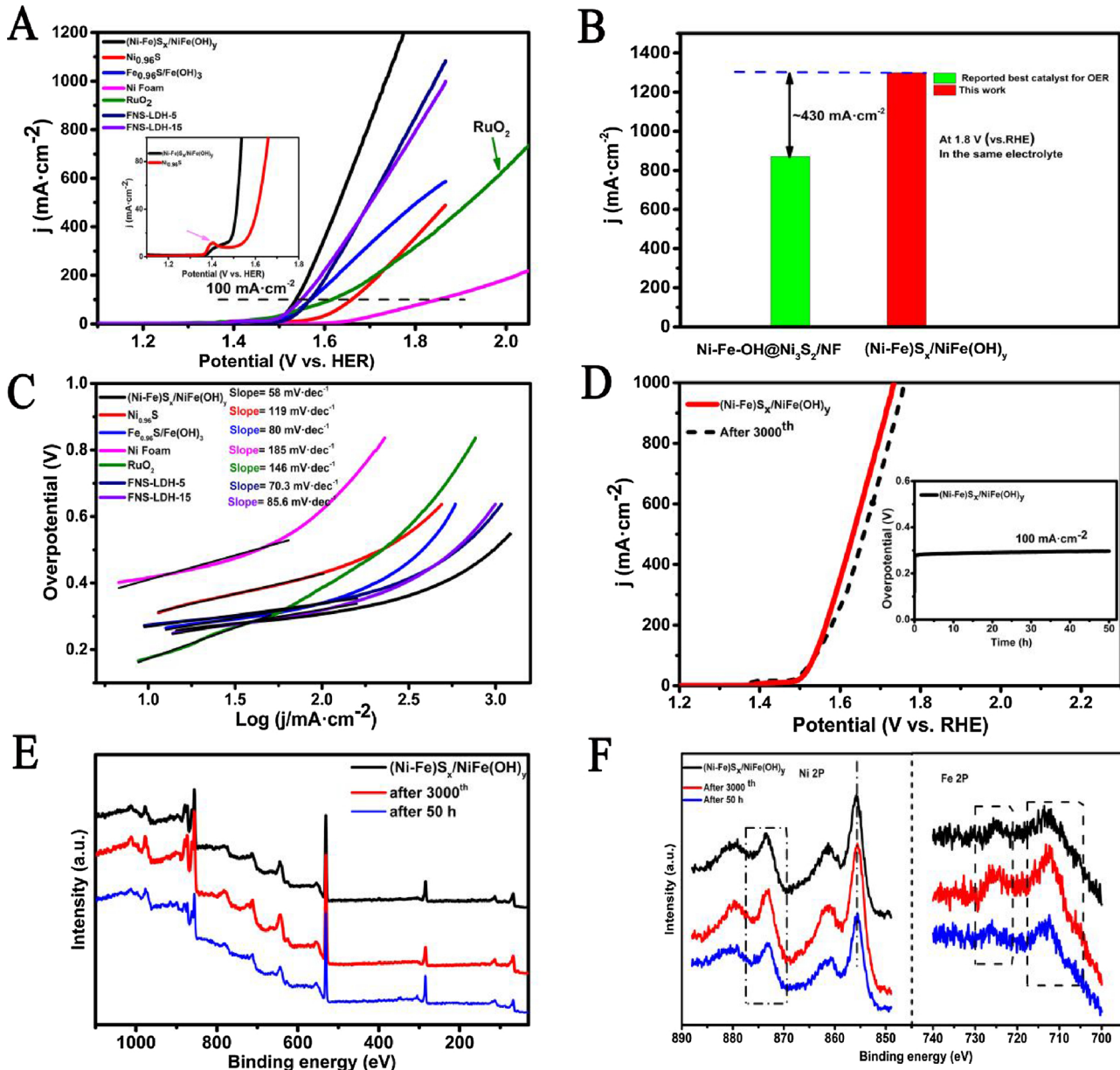


Fig. 5. OER performance at high-current-density in the presence of $(\text{Ni-Fe})\text{S}_x/\text{NiFe(OH)}_y$, $\text{Ni}_{0.96}\text{S}$, $\text{Fe}_{0.96}\text{S}/\text{Fe(OH)}_3$, FNS-LDH-5, FNS-LDH-15, RuO_2/NF , and Ni foam in (A) 1 M KOH solution without iR-compensations. (B) In comparison to reported best OER catalyst of $\text{Ni-Fe-OH@Ni}_3\text{S}_2/\text{NF}$ for OER activity [7]. (C) corresponding Tafel plots. (D) Polarization data for $(\text{Ni-Fe})\text{S}_x/\text{NiFe(OH)}_y$ before and after 3000 CV cycles, inset: chronopotentiometric curve under $100 \text{ mA}\cdot\text{cm}^{-2}$ for 50 h. (E) The XPS sum peaks, (F) Ni 2 P and Fe 2 P regions for $(\text{Ni-Fe})\text{S}_x/\text{NiFe(OH)}_y$ before and after 3000th as well as after 50 h measurements.

polarization curves of above samples with the inset of $\text{Ni}_{0.96}\text{S}$ and $(\text{Ni-Fe})\text{S}_x/\text{NiFe(OH)}_y$ within low current density of $100 \text{ mA}\cdot\text{cm}^{-2}$. There was distinct oxidation peak at $\sim 1.4 \text{ V}$ before the oxygen evolution for $\text{Ni}_{0.96}\text{S}$ but lack of $(\text{Ni-Fe})\text{S}_x/\text{NiFe(OH)}_y$, which can be explained electron-transfer from Ni^{2+} to Ni^{3+} in the materials to form active nickel (oxy)hydroxide phase [7,62]. the benchmarked RuO_2/NF catalyst for oxygen evolution, obviously displayed lower onset potential of 1.38 V . However, when the current density was over $80 \text{ mA}\cdot\text{cm}^{-2}$, a macroscopic phenomenon occurred that RuO_2 catalytic phase peeled off from NF, causing the whole RuO_2/NF electrode inactivation due to poor anchoring strength. Instead, in situ growing on NF self-support would not take place similar situation even at large-current-density ($\geq 1 \text{ A}\cdot\text{cm}^{-2}$) [7,47]. Compared with $\text{Ni}_{0.96}\text{S}$, the $\text{Fe}_{0.96}\text{S}/\text{Fe(OH)}_3$ catalyst exhibited significant OER electrocatalytic activity ($\eta_{100} = 341 \text{ mV}$) superior to defective $\text{Ni}_{0.96}\text{S}$ ($\eta_{100} = 430 \text{ mV}$), which can be well-defined explained to Fe-sites in metal-(oxy)hydroxide to be primary importance

for the OER [24,76]. With in the existence of both Ni^{2+} and Fe^{3+} , the optimized added Fe^{3+} concentration was 0.01 mol/L . To be exciting, the amorphous $(\text{Ni-Fe})\text{S}_x/\text{NiFe(OH)}_y$ composite exhibited best oxygen evolution activity ($\eta_{100} = 290 \text{ mV}$) among of the samples.

To more clearly understand the contributions of two components both Ni-Fe hydroxides and Ni-Fe sulfides in the $(\text{Ni-Fe})\text{S}_x/\text{NiFe(OH)}_y$ composite toward OER catalytic activity, as the Figure S11 displayed, we investigated the polarization curves of single and bimetallic Ni-Fe hydroxides. The single Fe(OH)_3 catalyst ($\eta_{200} = 390 \text{ mV}$) was inferior to bimetallic NiFe-OH ($\eta_{200} = 360 \text{ mV}$). There was evident difference at larger current density, indicating the good synergistic effect between Ni^{2+} and Fe^{3+} in Ni-Fe hydroxides at atomic level to enhance OER performance. Furthermore, the $\text{Fe}_{0.96}\text{S}/\text{Fe(OH)}_3$ nanosheet possessed lower OER overpotential than single Fe(OH)_3 due to its good conductivity from metal-like $\text{Fe}_{0.96}\text{S}$ with rich defects. As the facts of previous DFT calculations, ternary transition-metal sulfides possess higher

total density of states (TDOS) than binary sulfides at the Fermi leve, indicating the further enhanced electrical conductivity to be easier charge transfer [36,42]. Combined with our experimental results, it well confirmed that the wonderful OER activity can be ascribed to $(\text{Ni}-\text{Fe})\text{S}_x$ as the splendid electrical conductivity along with NiFe(OH)_y as synergetic highly-catalytic active phase. To be horizontal comparison, as the Fig. 5B shown, the newly reported best OER catalyst $(\text{Ni}-\text{Fe}-\text{OH}@\text{Ni}_3\text{S}_2/\text{NF})$ was $871 \text{ mA}\cdot\text{cm}^{-2}$ at 1.8 V in 1 KOH solution [7]. Under the same test conditions and potential, the current density of $(\text{Ni}-\text{Fe})\text{S}_x/\text{NiFe(OH)}_y$ was about 1.5 times higher than $\text{Ni}-\text{Fe}-\text{OH}@\text{Ni}_3\text{S}_2/\text{NF}$, indicating its OER “shining-lights”.

Further catalytic kinetics can be explored from Tafel slope, according to the four-electron transfer reaction pathways in alkaline solution for oxygen evolution as follows [77]:



the * representes the catalytically active site, where OH_* , O_* and HOO_* are the absorption-intermediates. As the Fig. 5C exhibited, the $(\text{Ni}-\text{Fe})\text{S}_x/\text{NiFe(OH)}_y$ catalyst exhibited the smallest Tafel slope of $58 \text{ mV}\cdot\text{decade}^{-1}$ in contrast to these $\text{Ni}_{0.96}\text{S}$ ($119 \text{ mV}\cdot\text{decade}^{-1}$), $\text{RuO}_2\text{-NF}$ ($146 \text{ mV}\cdot\text{decade}^{-1}$), $\text{Fe}_{0.96}\text{S}/\text{Fe(OH)}_3$ ($80 \text{ mV}\cdot\text{decade}^{-1}$), FNS-LDH-5 ($70.3 \text{ mV}\cdot\text{decade}^{-1}$), FNS-LDH-15 ($85.6 \text{ mV}\cdot\text{decade}^{-1}$), and NF ($185 \text{ mV}\cdot\text{decade}^{-1}$), respectively, implying a more rapid oxygen evolution charger transfer ability. To assess the catalytic stability of $(\text{Ni}-\text{Fe})\text{S}_x/\text{NiFe(OH)}_y$ catalyst, CV sweeps were conducted repeatedly in the range of 0.5 V to 1.56 V at the $50 \text{ mV}\cdot\text{s}^{-1}$. After 3000 cycles, negligible OER deactivation for $(\text{Ni}-\text{Fe})\text{S}_x/\text{NiFe(OH)}_y$ evidenced catalytic robustness (Fig. 5D). The chronopotentiometry (V-t) tested at $100 \text{ mA}\cdot\text{cm}^{-2}$ for at least 50 h further comfirmed super long-lasted stability with almost no potential loss. Further SEM and HR-TEM images indicated keeping well with its micro-tubes/spheres morphology and amorphous structures after 50 h durability test (Figure S12). In addition, the single $\text{Ni}_{0.96}\text{S}$ sample would almost fully be oxidated accompanying by release of SO_4^{2-} into electrolyte after constant current polarization of $100 \text{ mA}\cdot\text{cm}^{-2}$ for 50 h by XPS verified (Figure S13) in agreement with previous report [46], but the $(\text{Ni}-\text{Fe})\text{S}_x/\text{NiFe(OH)}_y$ showed little oxidation. The futher releasing contents of SO_4^{2-} (Tabel S4) proved this point by anionic chromatograph (ICS-900). It may be explained Fe-doping to form NiFe(OH)_y effectively reducing oxidation of metal-sulfur. In addition, The “Postmortem” XPS spectrum characterizations of $(\text{Ni}-\text{Fe})\text{S}_x/\text{NiFe(OH)}_y$ after 3000 CV cycles and 50 h continuous tests revealed no obvious evidences for the chemical structure changed for both Ni 2p and Fe 2p spectra (Fig. 5(E, F)). These results overall evinced excellent chemical stability of $(\text{Ni}-\text{Fe})\text{S}_x/\text{NiFe(OH)}_y$ during the electrocatalytic water oxidation.

3.4. Electrochemical water splitting

Motivated by the state-of-the-art HER and OER results, accordingly we assembled a two-electrode system by using $(\text{Ni}-\text{Fe})\text{S}_x/\text{NiFe(OH)}_y$ catalyst as both anode and cathode for overall water splitting. To the best of our knowledge, currently there are lack of regularly deep-investigations based on alkalinity and temperature impacting on the overall water-splitting catalytic activities as well as durability at large current density according to reported various bifunctional catalysts, which is urgently important to provide directly evidences for potential large-scale industrial applications. It is well-known that the theoretical potential of water-splitting is 1.23 V ($\Delta G = 237.2 \text{ kJ mol}^{-1}$) at 298 K [67]. According to Nernst equation, the alkalinity doesn't have effects on theoretical water decomposition voltage [78,79]. The Fig. 6A showed polarization curves of overall water-splitting on the strength of

different alkali concentrations range from 1 to 6 M KOH at 25°C . With the increase of alkalinity, at the beginning the water-splitting voltage significantly reduced up to 3 M KOH solution, then kept constant (e.g., overlap curves in 5 and 6 M KOH electrolyte). The $(\text{Ni}-\text{Fe})\text{S}_x/\text{NiFe(OH)}_y || (\text{Ni}-\text{Fe})\text{S}_x/\text{NiFe(OH)}_y$ electrodes achieved ultralow voltage 1.46 V at $10 \text{ mA}\cdot\text{cm}^{-2}$ in 1 M KOH electrolyte, superior to newly reported high active bifunctional catalysts, including FeMnP (1.55 V) [39], $\text{Ni}_{0.7}\text{Fe}_{0.3}\text{S}_2$ (1.63 V) [35], NiFeSP/NF (1.58 V) [80], $\text{Co}_1\text{Mn}_1\text{CH}/\text{NF}$ (1.68 V) [3], $\text{FeB}_2\text{-NF}$ (1.57 V) [19], $\text{Co}_{0.9}\text{S}_{0.58}\text{P}_{0.42}$ (1.59 V) [81], EG/ $\text{Co}_{0.85}\text{Se}/\text{NiFe-LDH}$ (1.67 V) [64], and P-NiFe (1.51 V) [27] et al.. Furthermore, the catalyst reached current density of $1 \text{ A}\cdot\text{cm}^{-2}$ only needing cell voltage of 2.32 V in 5 M KOH solution.

To clearly study the alkalinity impacting on overall water-splitting catalytic activity, we explored both HER and OER half-reaction catalytic activities in strong alkaline environment (5 M KOH solution). There are competitions between unfavorable HER kinetics and positive high ionic conductivity. As the Figure S14 exhibited, the HER activity both in 1 and 5 M KOH electrolyte almost kept unchangeableness, indicating cathodic water-reduction was not the cause of total overpotential reduction. Naturally, the anodic water-oxidation primarily resulted in such a low sum kinetic overpotential based on experimental facts (Figure S15), which were beneficial from rapid OER kinetics and enhanced conductivity under the high concentrated alkaline electrolyte. In addition, the industrial electrolyzers are commonly working at about $50\text{--}90^\circ\text{C}$ [82], such temperature providing several chances, like charge-transfer resistance decreased, lowered thermodynamical and kinetic overpotentials (from formula: $j = j_0 \exp(\frac{\alpha nF}{RT}(\eta))$) as well as facilitated H_2 and O_2 bubbles removal [79,83]. As shown in Fig. 6B, the cell voltage decreased with the increase of temperature range $25\text{--}80^\circ\text{C}$. For instance, $(\text{Ni}-\text{Fe})\text{S}_x/\text{NiFe(OH)}_y || (\text{Ni}-\text{Fe})\text{S}_x/\text{NiFe(OH)}_y$ electrodes exhibited low oneset voltage 1.39 V at $10 \text{ mA}\cdot\text{cm}^{-2}$ in 1 M KOH electrolyte at 40°C , even reaching 1.68 V at $100 \text{ mA}\cdot\text{cm}^{-2}$ compared with that 1.73 V at 25°C . The Fig. 6C uncovered both alkalinity and temperture to the effects of overall water splitting at fixed high current density of $1 \text{ A}\cdot\text{cm}^{-2}$. Based on above analysis, $(\text{Ni}-\text{Fe})\text{S}_x/\text{NiFe(OH)}_y || (\text{Ni}-\text{Fe})\text{S}_x/\text{NiFe(OH)}_y$ electrodes were carried out for electrochemical hydrolysis at optimized condition. The Fig. 6D exhibited ultra-low cell voltage of 2.12 V at $1 \text{ A}\cdot\text{cm}^{-2}$ in quasi-industrial environment (in 5 KOH & 60°C). Further overall hydrolysis durability measurements showed almost no loss of activity for 50 h at continuous $1000 \text{ mA}\cdot\text{cm}^{-2}$ (inset: Fig. 6D). After 50 h tests, the anodic material kept well with its chemical structure by Raman spectra indentified (inset: Fig. 6D). Above results amply proved the bifunctional $(\text{Ni}-\text{Fe})\text{S}_x/\text{NiFe(OH)}_y$ electrocatalyst may undertake large-scale industrial hydrolysis due to its super HER and OER catalytic activity along with excellent stability and low-cost fast synthetic method.

4. Conclusions

In summary, a new-type bifunctional amorphous $(\text{Ni}-\text{Fe})\text{S}_x/\text{NiFe(OH)}_y$ micro-tube/sphere films on NF substrate was fabricated by a simple one-step electron-induced co-deposited mechanism. Benefiting from hierarchical hollow micro-tube/sphere morphology and unique-particular amorphous architectures, the $(\text{Ni}-\text{Fe})\text{S}_x/\text{NiFe(OH)}_y$ composite exhibited splendid intrinsic HER activity with ultra-low overpotential of 124 mV at $100 \text{ mA}\cdot\text{cm}^{-2}$, even outstripping noble Pt sheets at $242 \text{ mA}\cdot\text{cm}^{-2}$ in the alkaline electrolyte. Together with excellent OER activity with current density of $1300 \text{ mA}\cdot\text{cm}^{-2}$ at 1.8 V superior to the reported best $\text{Ni}-\text{Fe}-\text{OH}@\text{Ni}_3\text{S}_2/\text{NF}$ catalyst, it is significant that a highly-efficient water electrolyzer was assembled by using $(\text{Ni}-\text{Fe})\text{S}_x/\text{NiFe(OH)}_y$ composite as both anode and cathode, exhibiting ultra-low voltage 1.46 V at $10 \text{ mA}\cdot\text{cm}^{-2}$ in 1 M KOH solution, even reaching large-current-density of $1 \text{ A}\cdot\text{cm}^{-2}$ only needed cell voltage of 2.12 V in quasi-industrial conditions along with keeping remarkable durability for 50 h with nearly no inactivation at $1000 \text{ mA}\cdot\text{cm}^{-2}$. This work not only displayed an exquisite morphology, multi-components control and

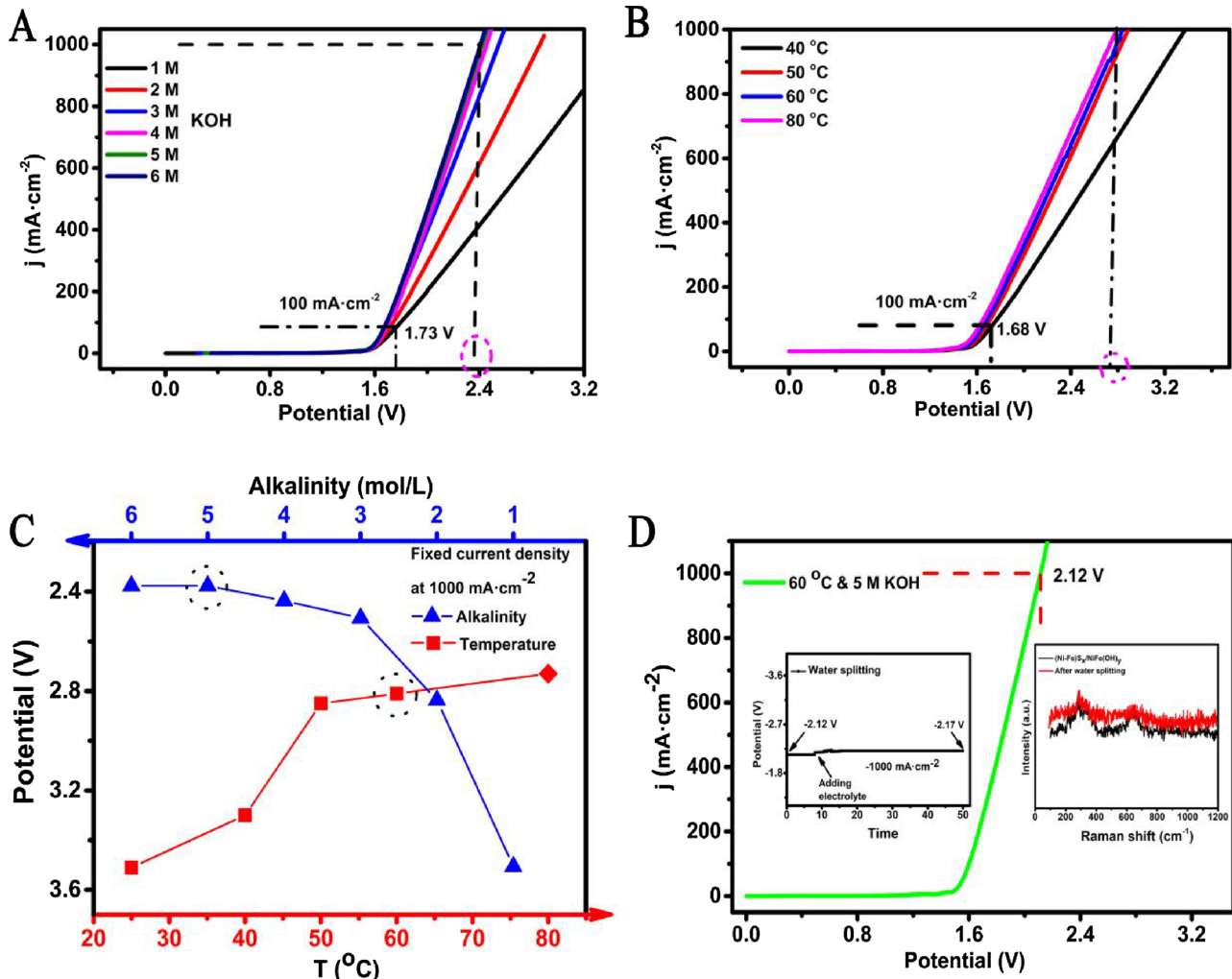


Fig. 6. Overall water-splitting performance based on the $(\text{Ni-Fe})\text{S}_x/\text{NiFe}(\text{OH})_y \parallel (\text{Ni-Fe})\text{S}_x/\text{NiFe}(\text{OH})_y$ electrodes. (A) Polarization curves depended on different alkali concentrations; (B) temperature contributions in 1 M KOH solution. (C) Water splitting potential plotted against both alkalinity and temperature in fixed current density of $1 \text{ A} \cdot \text{cm}^{-2}$. (D) Overall water splitting polarization curve of $(\text{Ni-Fe})\text{S}_x/\text{NiFe}(\text{OH})_y$ at 60°C and 5 M KOH solution, inset was the catalyst durability at fixed $1 \text{ A} \cdot \text{cm}^{-2}$ and anodic Raman spectrum after 50 h stability test.

phase evolution strategy for preparing low-cost and highly-active bi-functional electrocatalysts, but also provided direct evidences at large current density, implying potential large-scale industrial production.

Acknowledgment

The authors specially thank for the financial support of this work from the National Natural Science Foundation of China (51103120).

Appendix A. Supplementary data

Supplementary material related to this article can be found, in the online version, at doi:<https://doi.org/10.1016/j.apcatb.2019.01.082>.

References

- [1] M.S. Dresselhaus, I.L. Thomas, *Nature* 414 (2001) 332.
- [2] E. Hu, Y. Feng, J. Nai, D. Zhao, Y. Hu, X.W. Lou, *Energy Environ. Sci.* 11 (2018) 872–880.
- [3] T. Tang, W.J. Jiang, S. Niu, N. Liu, H. Luo, Y.Y. Chen, S.F. Jin, F. Gao, L.J. Wan, J.S. Hu, *J. Am. Chem. Soc.* 139 (2017) 8320–8328.
- [4] J. Yu, Q. Li, Y. Li, C.-Y. Xu, L. Zhen, V.P. Dravid, J. Wu, *Adv. Funct. Mater.* 26 (2016) 7644–7651.
- [5] H. Congling, Z. Lei, Z. Zhi-Jian, L. Ang, C. Xiaoxia, G. Jinlong, *Adv. Mater.* 30 (2018) 1705538.
- [6] H. Zhu, J. Zhang, R. Yanzhang, M. Du, Q. Wang, G. Gao, J. Wu, G. Wu, M. Zhang, B. Liu, J. Yao, X. Zhang, *Adv. Mater.* 27 (2015) 4752–4759.
- [7] Z. Xu, L. Yipu, L. Guo-Dong, W. Yuan Yuan, L. Da-Peng, L. Wang, L. Hai-Wen, W. Dejun, Z. Yu, Z. Xiaoxin, *Adv. Mater.* 29 (2017) 1700404.
- [8] R. Wu, J. Zhang, Y. Shi, D. Liu, B. Zhang, *J. Am. Chem. Soc.* 137 (2015) 6983–6986.
- [9] F. Yang, Y. Zhao, Y. Du, Y. Chen, G. Cheng, S. Chen, W. Luo, *Adv. Energy Mater.* 8 (2018) 1703489.
- [10] Y. Lei, S. Pakhira, K. Fujisawa, X. Wang, O.O. Iyiola, N. Perea Lopez, A. Laura Elias, L. Pulickal Rajkumar, C. Zhou, B. Kabius, N. Alem, M. Endo, R. Lv, J.L. Mendoza-Cortes, M. Terrones, *ACS Nano* 11 (2017) 5103–5112.
- [11] J. Xie, H. Zhang, S. Li, R. Wang, X. Sun, M. Zhou, J. Zhou, X.W. Lou, Y. Xie, *Adv. Mater.* 25 (2013) 5807–5813.
- [12] J.-X. Feng, J.-Q. Wu, Y.-X. Tong, G.-R. Li, *J. Am. Chem. Soc.* 140 (2018) 610–617.
- [13] X. Fan, Y. Liu, Z. Peng, Z. Zhang, H. Zhou, X. Zhang, B.I. Yakobson, W.A. Goddard 3rd, X. Guo, R.H. Hauge, J.M. Tour, *ACS Nano* 11 (2017) 384–394.
- [14] Y. Huang, Q. Gong, X. Song, K. Feng, K. Nie, F. Zhao, Y. Wang, M. Zeng, J. Zhong, Y. Li, *ACS Nano* 10 (2016) 11337–11343.
- [15] M.Y. Zu, P.F. Liu, C. Wang, Y. Wang, L.R. Zheng, B. Zhang, H. Zhao, H.G. Yang, *ACS Energy Lett.* 3 (2017) 78–84.
- [16] J. Tian, Q. Liu, A.M. Asiri, X. Sun, *J. Am. Chem. Soc.* 136 (2014) 7587–7590.
- [17] R. Zhang, X. Wang, S. Yu, T. Wen, X. Zhu, F. Yang, X. Sun, X. Wang, W. Hu, *Adv. Mater.* (2016).
- [18] T. Liu, X. Ma, D. Liu, S. Hao, G. Du, Y. Ma, A.M. Asiri, X. Sun, L. Chen, *ACS Catal.* (2016) 98–102.
- [19] H. Li, P. Wen, Q. Li, C. Dun, J. Xing, C. Lu, S. Adhikari, L. Jiang, D.L. Carroll, S.M. Geyer, *Adv. Energy Mater.* 7 (2017) 1700513.
- [20] J. Masa, P. Weide, D. Peeters, I. Sinev, W. Xia, Z. Sun, C. Somsen, M. Muhler, W. Schuhmann, *Adv. Energy Mater.* 6 (2016) 1502313.
- [21] Y. Zheng, Y. Jiao, Y. Zhu, L.H. Li, Y. Han, Y. Chen, A. Du, M. Jaroniec, S.Z. Qiao, *Nat. Commun.* 5 (2014) 3783.
- [22] J.X. Feng, H. Xu, S.H. Ye, G. Ouyang, Y.X. Tong, G.R. Li, *Angew. Chem., Int. Ed.* 56 (2017) 8120–8124.

[23] Y. Jin, H. Wang, J. Li, X. Yue, Y. Han, P.K. Shen, Y. Cui, *Adv. Mater.* 28 (2016) 3785–3790.

[24] M. Gorlin, P. Chernev, J. Ferreira de Araujo, T. Reier, S. Dresp, B. Paul, R. Krahnen, H. Dau, P. Strasser, *J. Am. Chem. Soc.* 138 (2016) 5603–5614.

[25] L. Han, X.Y. Yu, W. Lou Xiong, *Adv. Mater.* 28 (2016) 4601–4605.

[26] H. Liang, F. Meng, M. Cabán-Acevedo, L. Li, A. Forticaux, L. Xiu, Z. Wang, S. Jin, *Nano Lett.* 15 (2015) 1421–1427.

[27] F.-S. Zhang, J.-W. Wang, J. Luo, R.-R. Liu, Z.-M. Zhang, C.-T. He, T.-B. Lu, *Chem. Sci.* 9 (2018) 1375–1384.

[28] Y. Li, C. Zhao, *Chem. Mater.* 28 (2016) 5659–5666.

[29] J. Suntivich, K.J. May, H.A. Gasteiger, J.B. Goodenough, Y. Shao-Horn, *Science* 334 (2011) 1383.

[30] H. Shi, H. Liang, F. Ming, Z. Wang, *Angew. Chem., Int. Ed.* 129 (2016) 588–592.

[31] I. Roger, M.A. Shipman, M.D. Symes, *Nat. Rev. Chem.* 1 (2017) 0003.

[32] D.G. Nocera, *Acc. Chem. Res.* 45 (2012) 767–776.

[33] C.G. Morales-Guio, L.-A. Stern, X. Hu, *Chem. Soc. Rev.* 43 (2014) 6555–6569.

[34] T. Liu, A.M. Asiri, X. Sun, *Nanoscale* 8 (2016) 3911–3915.

[35] J. Yu, G. Cheng, W. Luo, *J. Mater. Chem. A* 5 (2017) 15838–15844.

[36] Y. Tang, H. Yang, J. Sun, M. Xia, W. Guo, L. Yu, J. Yan, J. Zheng, L. Chang, F. Gao, *Nanoscale* 10 (2018) 10459–10466.

[37] C. Du, L. Yang, F. Yang, G. Cheng, W. Luo, *ACS Catal.* 7 (2017) 4131–4137.

[38] H. Liang, A.N. Gandhi, D.H. Anjum, X. Wang, U. Schwingenschlogl, H.N. Alshareef, *Nano Lett.* 16 (2016) 7718–7725.

[39] Z. Zhao, D.E. Schipper, A.P. Leitner, H. Thirumalai, J.-H. Chen, L. Xie, F. Qin, M.K. Alam, L.C. Grabow, S. Chen, D. Wang, Z. Ren, Z. Wang, K.H. Whitmire, J. Bao, *Nano Energy* 39 (2017) 444–453.

[40] C. Du, M. Shang, J. Mao, W. Song, *J. Mater. Chem. A* 5 (2017) 15940–15949.

[41] Y. Zheng, Y. Jiao, M. Jaroniec, S.Z. Qiao, *Angew. Chem., Int. Ed.* 54 (2015) 52–65.

[42] D.Y. Wang, M. Gong, H.L. Chou, C.J. Pan, H.A. Chen, Y. Wu, M.C. Lin, M. Guan, J. Yang, C.W. Chen, Y.L. Wang, B.J. Hwang, C.C. Chen, H. Dai, *J. Am. Chem. Soc.* 137 (2015) 1587–1592.

[43] X. Ge, L. Chen, L. Zhang, Y. Wen, A. Hirata, M. Chen, *Adv. Mater.* 26 (2014) 3100–3104.

[44] C.G. Morales-Guio, X. Hu, *Acc. Chem. Res.* 47 (2014) 2671–2681.

[45] Y. Rao, H. Ning, X. Ma, Y. Liu, Y. Wang, H. Liu, J.L. Liu, Q.S. Zhao, M.B. Wu, *Carbon* 129 (2018) 335–341.

[46] O. Mabayoje, A. Shoola, B.R. Wygant, C.B. Mullins, *ACS Energy Lett.* 1 (2016) 195–201.

[47] K.N. Dinh, P. Zheng, Z. Dai, Y. Zhang, R. Dangol, Y. Zheng, B. Li, Y. Zong, Q. Yan, *Small* 14 (2018) 1703257.

[48] Y. Jin, S. Huang, X. Yue, H. Du, P.K. Shen, *ACS Catal.* 8 (2018) 2359–2363.

[49] L. Wang, J. Geng, W. Wang, C. Yuan, L. Kuai, B. Geng, *Nano Res.* 8 (2015) 3815–3822.

[50] Y. Liu, G. Yu, G.D. Li, Y. Sun, T. Asefa, W. Chen, X. Zou, *Angew. Chem., Int. Ed.* 54 (2015) 10752–10757.

[51] S.-Q. Liu, H.-R. Wen, G. Ying, Y.-W. Zhu, X.-Z. Fu, R. Sun, C.-P. Wong, *Nano Energy* 44 (2018) 7–14.

[52] J. Shi, X. Li, G. He, L. Zhang, M. Li, J. Mater. Chem. A 3 (2015) 20619–20626.

[53] J.-Y. Lin, J.-H. Liao, S.-W. Chou, *Electrochim. Acta* 56 (2011) 8818–8826.

[54] A. Ghahremaninezhad, E. Asselin, D.G. Dixon, *J. Phys. Chem. C* 115 (2011) 9320–9334.

[55] C. Yuan, J. Li, L. Hou, X. Zhang, L. Shen, W. Lou Xiong, *Adv. Funct. Mater.* 22 (2012) 4592–4597.

[56] X. Lu, C. Zhao, *Nat. Commun.* 6 (2015) 6616.

[57] N. Han, K.R. Yang, Z. Lu, Y. Li, W. Xu, T. Gao, Z. Cai, Y. Zhang, V.S. Batista, W. Liu, X. Sun, *Nat. Commun.* 9 (2018) 924.

[58] Q. Liu, J. Tian, W. Cui, P. Jiang, N. Cheng, M. Asiri Abdullah, X. Sun, *Angew. Chem., Int. Ed.* 53 (2014) 6710–6714.

[59] F. Wang, P. He, Y. Li, T.A. Shifa, Y. Deng, K. Liu, Q. Wang, F. Wang, Y. Wen, Z. Wang, X. Zhan, L. Sun, J. He, *Adv. Funct. Mater.* (2017) 1605802.

[60] D.W. Bishop, P.S. Thomas, A.S. Ray, Elsevier Sci. Ltd. 33 (1998) 1303–1306.

[61] W.D. Chemelewski, H.-C. Lee, J.-F. Lin, A.J. Bard, C.B. Mullins, *J. Am. Chem. Soc.* 136 (2014) 2843–2850.

[62] M.W. Louie, A.T. Bell, *J. Am. Chem. Soc.* 135 (2013) 12329–12337.

[63] L. Yu, H. Zhou, J. Sun, F. Qin, F. Yu, J. Bao, Y. Yu, S. Chen, Z. Ren, *Energy Environ. Sci.* 10 (2017) 1820–1827.

[64] Y. Hou, M.R. Lohe, J. Zhang, S. Liu, X. Zhuang, X. Feng, *Energy Environ. Sci.* 9 (2016) 478–483.

[65] X. Long, G. Li, Z. Wang, H. Zhu, T. Zhang, S. Xiao, W. Guo, S. Yang, *J. Am. Chem. Soc.* 137 (2015) 11900–11903.

[66] T. Liu, F. Yang, G. Cheng, W. Luo, *Small* 14 (2018) 1703748.

[67] Z. Zhu, H. Yin, C.-T. He, M. Al-Mamun, P. Liu, L. Jiang, Y. Zhao, Y. Wang, H.-G. Yang, Z. Tang, D. Wang, X.-M. Chen, H. Zhao, *Adv. Mater.* 30 (2018) 1801171.

[68] Y. Lin, L. Yang, Y. Zhang, H. Jiang, Z. Xiao, C. Wu, G. Zhang, J. Jiang, L. Song, *Adv. Energy Mater.* 8 (2018) 1703623.

[69] X. Wang, W. Ma, C. Ding, Z. Xu, H. Wang, X. Zong, C. Li, *ACS Catal.* 8 (2018) 9926–9935.

[70] Y. Li, H. Zhang, M. Jiang, Q. Zhang, P. He, X. Sun, *Adv. Funct. Mater.* 27 (2017) 1702513.

[71] F. Yang, Y. Chen, G. Cheng, S. Chen, W. Luo, *ACS Catal.* 7 (2017) 3824–3831.

[72] R. He, J. Hua, A. Zhang, C. Wang, J. Peng, W. Chen, J. Zeng, *Nano Lett.* 17 (2017) 4311–4316.

[73] G. Zhang, Y.-S. Feng, W.-T. Lu, D. He, C.-Y. Wang, Y.-K. Li, X.-Y. Wang, F.-F. Cao, *ACS Catal.* 8 (2018) 5431–5441.

[74] H. Zhou, F. Yu, J. Sun, H. Zhu, I.K. Mishra, S. Chen, Z. Ren, *Nano Lett.* 16 (2016) 7604–7609.

[75] Y. Guo, L. Gan, C. Shang, E. Wang, J. Wang, *Adv. Funct. Mater.* (2016) 1602699.

[76] T. Shinagawa, A.T. Garcia-Esparza, K. Takanabe, *Sci. Rep.* 5 (2015) 13801.

[77] Y. Wang, B. Kong, D. Zhao, H. Wang, C. Selomulya, *Nano Today* 15 (2017) 26–55.

[78] F. Wang, T.A. Shifa, X. Zhan, Y. Huang, K. Liu, Z. Cheng, C. Jiang, J. He, *Nanoscale* 7 (2015) 19764–19788.

[79] C. Xiang, K.M. Papadantonakis, N.S. Lewis, *Mater. Horiz.* 3 (2016) 169–173.

[80] Y. Xin, X. Kan, L.Y. Gan, Z. Zhang, *ACS Nano* 11 (2017) 10303–10312.

[81] Z. Dai, H. Geng, J. Wang, Y. Luo, B. Li, Y. Zong, J. Yang, Y. Guo, Y. Zheng, X. Wang, Q. Yan, *ACS Nano* 11 (2017) 11031–11040.

[82] S. Piontek, C. Andronescu, A. Zaichenko, B. Konkena, K. Junge Puring, B. Marler, H. Antoni, I. Sinev, M. Muhler, D. Mollenhauer, B. Roldan Cuenya, W. Schuhmann, U.-P. Apfel, *ACS Catal.* 8 (2018) 987–996.

[83] T.P. Heins, N. Harms, L.-S. Schramm, U. Schröder, *Energy Technol.* 4 (2016) 1509–1513.